RSC Advances

PAPER

View Article Online
View Journal | View Issue

Cite this: *RSC Adv.*, 2026, **16**, 16418

Chirality-promoted photocatalysis: a strategic framework for advancing future dye degradation technologies

Utpal Kumar Gosh, Anujit Balo and Koyel Banerjee Ghosh *

Received 25th January 2026
Accepted 20th March 2026

DOI: 10.1039/d6ra00665e

rsc.li/rsc-advances

Photocatalysis has emerged as a promising approach for the degradation of dyes. However, the role of the oxygen reduction reaction (ORR) in this process has not been thoroughly explored, despite being a fundamental process in dye degradation. In this work, we explore the influence of chirality-induced spin-polarization in the photocatalyst and its subsequent impact on the kinetics of photocatalytic dye degradation. We use here cysteine-directed chiral gold nanoparticles as spin-polarized photocatalysts and demonstrate the enhancement of ORR activity, which indirectly accelerates the kinetics of degradation of both cationic Rhodamine B and anionic Methyl Orange dye. Comparative studies with achiral gold nanoparticles highlight the crucial role of spin polarization in modulating photocatalytic efficiency. This study establishes a generic strategy for optimising dye degradation irrespective of their structure by combining spin effects with photocatalysis, offering new insights into the design of advanced materials for environmental restoration.

Introduction

The mitigation of dye contaminants in industrial wastewater, which is discharged into natural water systems, is essential, as these pollutants pose serious threats to aquatic ecosystems and present potential carcinogenic hazards to humans.[1,2] Numerous techniques have been explored for dye removal. Among them, photocatalysis has emerged as a promising approach.[3–5] However, certain important factors that influence photocatalytic activity, such as the oxygen reduction reaction (ORR), have not been thoroughly investigated in this context. The fundamental mechanism of photocatalytic dye degradation involves three main steps. First, when photons with energy greater than the catalyst's bandgap are absorbed, electron–hole pairs are generated as electrons transition take place from the valence band to the conduction band, resulting in the formation of positively charged holes. Second, these excited electrons in the conduction band and the positive holes in the valence band engage in redox reactions with surface-adsorbed water and oxygen, producing reactive radicals like hydroxyl ($OH^{\cdot}$). Finally, the generated hydroxyl radicals oxidize the dye molecules, degrading them into smaller, non-toxic products such as carbon dioxide and other benign byproducts.[6] Therefore, the rapid formation of hydroxyl radicals under light irradiation plays a key role in enhancing photocatalytic efficiency. In most studies, the underlying principle for the evolution of photocatalysts is mainly focused on tuning the electronic structure, as it is obvious that, thermodynamically, it is the main controlling factor for catalysis.[7–10] However, other unconventional factors, such as considerations of spin effects, cannot be overlooked, as they have been shown to play a decisive role in the reduction of triplet oxygen.[11–15] In this study, we regulate the oxygen reduction reaction by introducing spin polarization into the photocatalyst and investigate its influence on the kinetics of dye degradation. In our previous work, we examined spin-polarized catalysts for the electrochemical oxygen reduction reaction, considering its importance in metal–air batteries and fuel cell applications.[16–18] Spin-polarization can be introduced in the catalyst either by employing chiral molecules or by using magnetic materials as the catalyst. Chiral molecules show spin selectivity due to the chiral-induced spin selectivity (CISS) effect, as established earlier.[19–25] However, the impact of spin-polarization on the photocatalyst has not been explored yet.

In this study, we employ cysteine-directed chiral gold nanoparticles as spin-polarized photocatalysts to investigate their influence on the degradation kinetics of Rhodamine B (RhB) and Methyl Orange (MO) dyes. The rationale behind opting for these dyes is to investigate and establish a generic way to improve the kinetics of dye degradation, as Rhodamine B is a cationic dye, and Methyl Orange is an anionic dye, and they both are known for their industrial usage. The impact of spin polarization is assessed by comparing the photocatalytic activity of chiral and achiral cysteine-modified gold nanoparticles.

Results and discussion

Characterization of the gold nanoparticles

Cysteine-encoded chiral and achiral gold nanoparticles were synthesized following the procedure reported elsewhere.[26] A

Department of Chemistry, Indian Institute of Technology Hyderabad, Telangana 502284, India. E-mail: koyel@chy.iith.ac.in

brief discussion is given in the experimental section in the SI. After the synthesis, the particles were characterized using X-ray diffraction (XRD). The XRD patterns of as-prepared cystine-capped Au NPs match well with the standard cubic crystal structure without any impurities, as shown in Fig. 1a. The diffraction pattern indicates the existence of (111), (200), (220), and (311) planes, identified by the peaks at 38.44°, 44.60°, 64.71°, and 77.62°, respectively. This finding is consistent with the standard JCPDS file number 04-0784. UV-Visible (UV-Vis) absorption spectroscopy was employed to investigate the optical properties of the Au NPs, which display distinct absorbance bands at 534 nm as revealed in Fig. 1b. The circular dichroism (CD) spectra shown in Fig. 1c reveal the strong signals with opposite polarizability for chiral L- and D-Au NPs, whereas the achiral Au NPs are CD silent. The correspondence between the mirror image CD signals and the UV-Vis absorption peaks indicates the successful construction of L- and D-Au NPs. However, as reported by Hammer *et al.* and other groups that D-cysteine has a stronger binding capability compared to that of L-cysteine on the surface of Au (17 11 9)^{S}, the *g*-factor values (as presented in Fig. S1) differ for L- and D-cysteine modified Au-nanoparticles, despite the same concentration of D-, and L-cysteine molecules.[26–28] To evaluate the morphology of the Au NPs, transmission electron microscopy (TEM) and scanning electron microscopy (SEM) have been conducted. The TEM image (Fig. 1d and S2a) reveals distortion of edges oriented along a specific direction in the case of chiral (L- or D-) Au NPs, which can be attributed to the enantioselective binding of cysteine molecules. In contrast, when DL-cysteine was interacted, the edges exhibited symmetric distortion in both directions, resulting in a round-shaped nanoparticle morphology (Fig. S2b). These structural differences are consistent with the trends observed in the CD spectra and the previously reported literature.[26] Complementary SEM images (Fig. S3, SI) further confirm the presence of uniformly distributed Au NPs with distorted edges, supporting the role of enantioselective cysteine interactions in shaping nanoparticle morphology.

Photocatalytic study

The photocatalytic activities were carried out in a 15 mL borosilicate glass vessel. 150 μl (with absorbance 0.2 a.u.) of chiral L- or D-Au NPs were dispersed in 3 mL of RhB solution in water. To evaluate the influence of varying pollution levels on catalytic performance, photocatalytic degradation experiments were

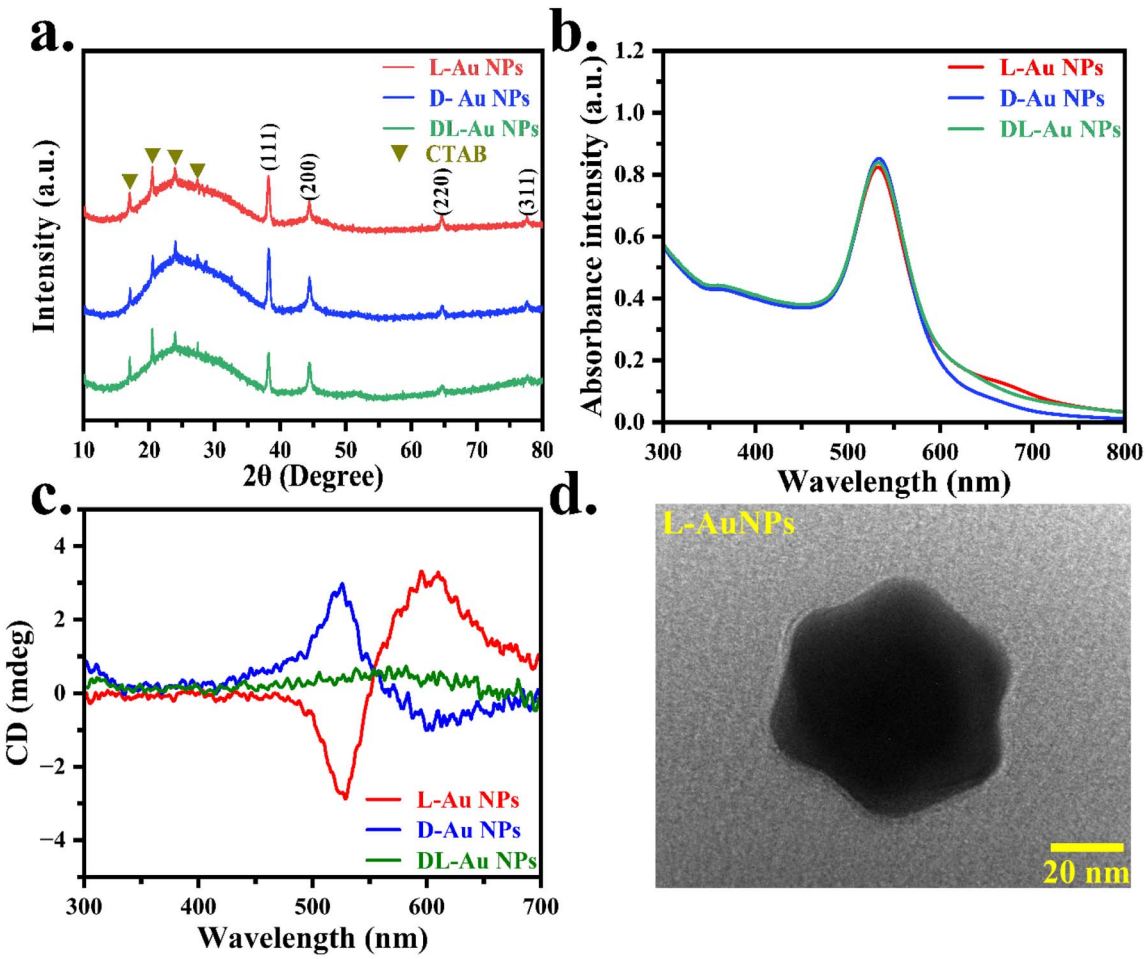

Fig. 1 Structural and optical analysis of the photocatalyst. (a) XRD spectra, (b) UV-Vis spectra, and (c) CD spectra of L-Au NPs (red), D-Au NPs (blue), and DL-Au NPs (green). (d) TEM image of L-Au NPs with the scale bar of 20 nm.

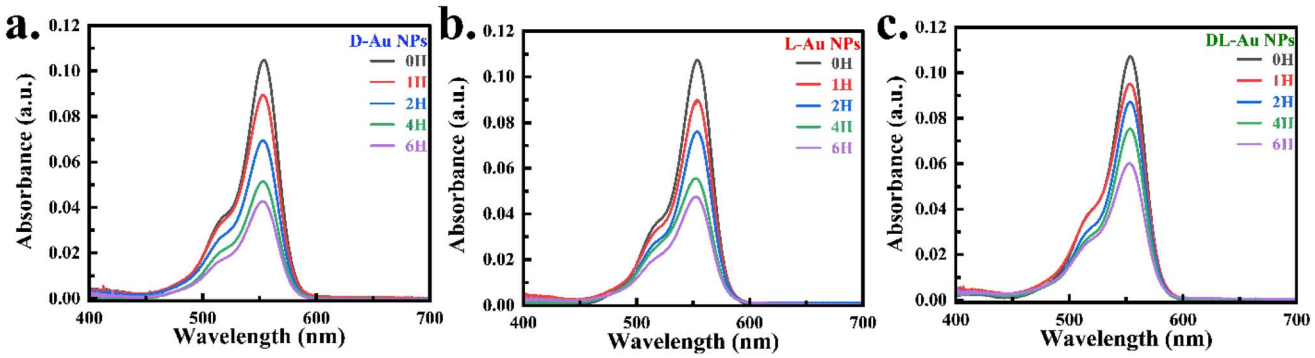

Fig. 2 RhB degradation kinetics. UV-Vis spectra of 1 μM RhB degradation by (a) D-, (b) L-, and (c) DL-Au NPs at different times.

conducted using Rhodamine B at concentrations of 0.5, 1, and 2 μM. After purging oxygen gas for ten minutes, the glass tube was sealed with an O_2 balloon and kept in the dark for thirty minutes to reach equilibrium. The reaction mixture was stirred under irradiation with a 27 W white LED at room temperature. Continuous cold air was made to flow through the laboratory-made photo chamber to maintain the temperature of the reaction mixture at ~25 °C throughout the experiment. The photocatalytic reaction was performed for 1 h, 2 h, 4 h, and 6 h. After centrifuging the reaction mixture, the concentration of the remaining dye was determined using UV-Vis spectroscopy.

The absorption spectra recorded at different time intervals for the RhB (1 μM) degradation employing chiral and achiral Au NPs are presented in Fig. 2a–c. As expected with increasing reaction time, the characteristic absorption peaks of RhB (at $\lambda_{max} = 554$ nm) decline gradually, revealing the decrease in the concentration of the dye. However, the decrease in concentration of RhB is different for chiral and achiral catalysts. The reaction kinetics and corresponding degradation efficiencies are presented in Fig. 3. The plots of the negative logarithm of (C_t/C_0) with the reaction time are shown in Fig. 3a, which reveal that the rate of reaction is first order with respect to dye concentration. The degradation efficiency (D), shown in Fig. 3b has been calculated according to the following equation.

$$D = \frac{C_0 - C_t}{C_0} \times 100\% \quad (1)$$

Here, C_t (mol L^{-1}) is the concentration of the organic dye measured at time t, and C_0 (mol L^{-1}) is the initial concentration of the organic dye before irradiation. The concentration was determined from the intensity of the absorbance maxima using the Lambert–Beer law. Further, photocatalytic degradation experiments were performed for RhB at initial concentrations of 0.5 and 2 μM, and the results followed trends consistent with those observed at 1 μM, as shown in Fig. S4–S7. In all cases, it has been found that the chiral catalyst has superior dye degradation efficiency than the achiral one. This contrast is further supported by the kinetic analysis when calculating the specific reaction rate or rate constant, as illustrated in Fig. 4. The decline in degradation efficiency and rate constant with increasing initial dye concentration can be attributed to multiple factors. First, the limited number of active sites on the catalyst leads to competitive adsorption at higher dye concentrations. Second, stronger light absorption by the dye reduces

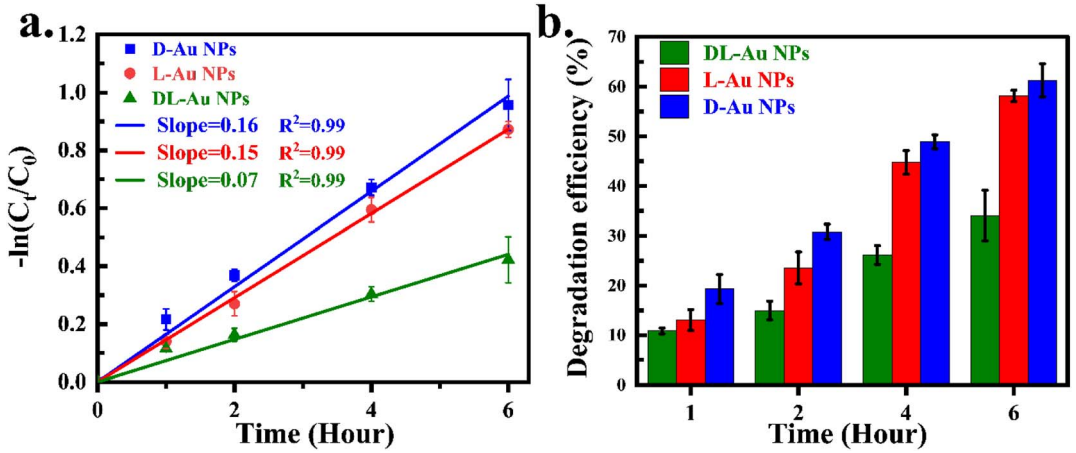

Fig. 3 Time-dependent photocatalytic activity study. (a) Kinetics ($-\ln(C_t/C_0)$ with respect to time (h)) plot of 1 μM RhB under visible light exposure. (b) Comparison of 1 μM RhB degradation efficiency *vs.* time for D-, L-, and DL-Au NPs photocatalyst. The experiments were repeated three times independently to check the reproducibility, and the error bars include the uncertainty in the experiments.

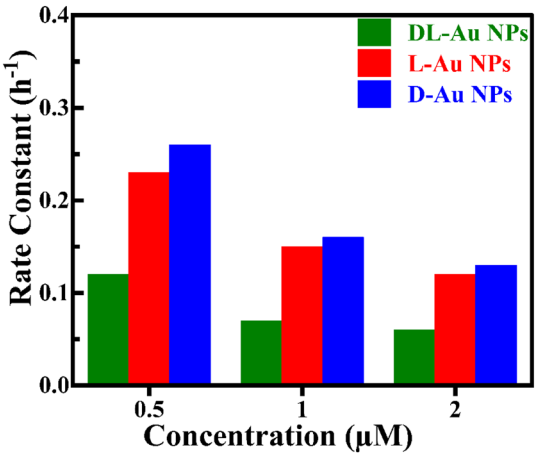

Fig. 4 Chiral advantages study for RhB degradation. Rate constant (h^{-1}) with respect to concentration (μM) plot for D-, L-, and DL-Au NPs photocatalyst.

light penetration, thereby decreasing the photon flux reaching the catalyst surface and lowering the effective generation of reactive radicals responsible for degradation. However, the chiral catalyst consistently exhibits higher catalytic activity than DL-Au nanoparticles across all tested conditions, indicating that its chiral advantage is preserved over a broad range of pollutant concentrations.

A similar approach was followed to study the degradation of MO. However, the photocatalytic experiment was performed for 3 h, 6 h, and 12 h for MO (12 μM) due to its higher stability. A similar type of observation is found for the degradation of Methyl Orange. Though the degradation rate of MO is lower with respect to RhB, the chiral Au NPs outperform the achiral Au NPs in terms of catalytic activity for the degradation of MO. Fig. 5a–c shows that the characteristic peak intensity of the MO (at $\lambda_{max} = 464$ nm) is getting reduced due to degradation under illumination in the presence of chiral and achiral catalysts. Fig. 6a shows that the reaction rate is first order with respect to the MO dye concentration. The rate constants analyzed from the data are higher for the chiral catalyst in comparison with the achiral one. The degradation efficiency determined from eqn (1) for MO also reveals enhanced kinetics of degradation while using chiral L- or D-Au NPs (Fig. 6b). The photocatalytic dye degradation experiments with two different dyes using catalysts from the same synthesized batch were independently repeated three times to verify reproducibility. The error bars in the plots represent the experimental uncertainty associated with these measurements. A detailed table of error bar values is provided in the SI, Tables S1–S4.

We have carried out the control experiment to reveal the stability of RhB and MO dyes in the presence of light and oxygen, but without any catalyst. Slight degradation of RhB is observed over the duration of illumination for 6H. However, almost no degradation is found for MO even when it was illuminated for 12 hours. The data is shown in SI (Fig. S8). Control experiments were conducted using a non-chiral thiolated molecule, mercaptopropionic acid. The results exhibited a trend similar to that observed for DL-cysteine-modified Au nanoparticles, as shown in Fig. S9. This supports the conclusion that the differences observed between L- and D-cysteine systems arise from chirality rather than general surface chemistry effects. Post-catalysis characterization was performed by recovering the catalyst after the photocatalytic reaction carried out for RhB for 6 h and analyzing it using Fourier Transform Infrared Spectroscopy (FTIR) and X-ray Photoelectron Spectroscopy (XPS), as shown in Fig. S10. The results confirm that the catalyst retained its structural integrity, demonstrating good stability under the reaction conditions.

Plausible mechanism

In the process of photocatalytic dye degradation utilizing chiral plasmonic gold nanoparticles, the initial steps start with the excitation of localized surface plasmons upon exposure to light. This resonance generates high-energy charge carriers within nanoparticles. These energetic carriers play a significant role in initiating and mediating redox reactions at the nanoparticle surface.[5] The electrons in the conduction band are transferred to the adsorbed oxygen molecules, (O_2) in a spin-specific way due to the CISS effect and get reduced to superoxide radicals ($O_2^{\cdot -}$). Simultaneously, the positive holes in the valence band oxidize the water molecules, (H_2O) or hydroxide ions (OH^-) that are bound to the surface and form hydroxyl radicals ($HO^{\cdot}$), which are highly reactive oxidants. These reactive oxygen

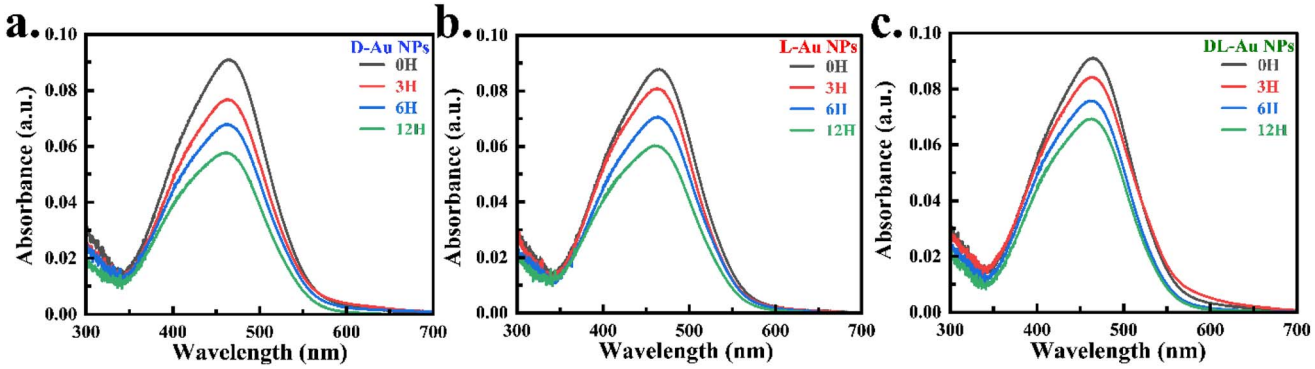

Fig. 5 MO degradation kinetics. UV-Vis spectra of MO degradation by (a) D-, (b) L-, and (c) DL-Au NPs at different time.

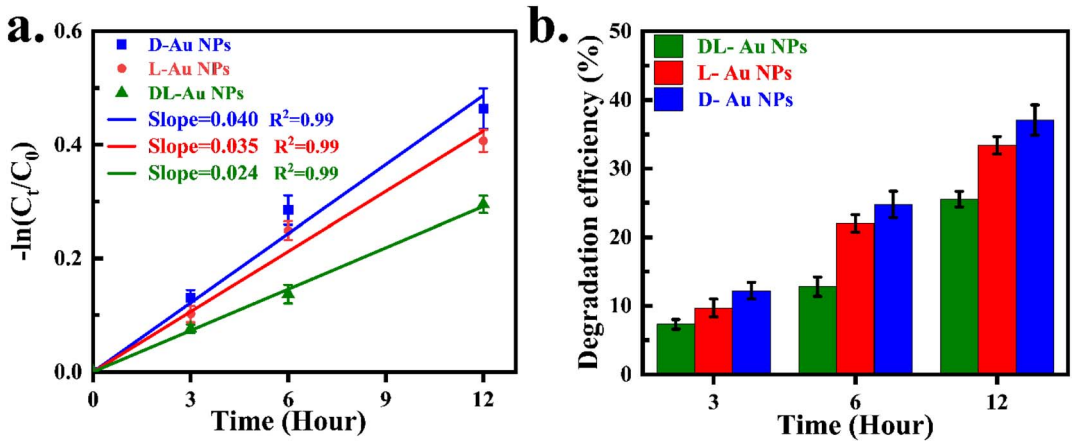

Fig. 6 Time-dependent photocatalytic activity study for MO degradation. (a) Kinetics ($-\ln(C_t/C_0)$ with respect to time (h)) plot of MO under visible light exposure. (b) Comparison of MO degradation efficiency *vs.* time for D-, L-, and DL-Au NPs photocatalyst. The experiments were repeated three times independently to ensure reproducibility, and the error bars represent the experimental uncertainty associated with these measurements.

species not only contribute to further oxidation steps but also enhance the catalytic cycle by mitigating electron–hole recombination. The superoxide radicals ($O_2^{\cdot -}$) generated on the surface of nanoparticles undergo protonation and form hydroperoxyl radicals ($HOO^{\cdot}$), and they subsequently transform into hydrogen peroxide (H_2O_2). Then, H_2O_2 decomposes into highly reactive $HO^{\cdot}$ radicals, enhancing the oxidative potential of the system. Together, these reactive species further oxidize dye molecules adsorbed on or near the catalyst surface, breaking them down into tiny intermediates. Through a series of oxidation processes, these intermediates finally mineralize into neutral end-products like water (H_2O), carbon dioxide (CO_2), *etc.* The plausible mechanism is shown in Scheme 1. The role of chirality is to induce the spin-polarization that facilitates the transfer of an electron to triplet oxygen, which is the step of the reaction mechanism.

$$O_2(ads) + e^- \rightarrow O_2^{\cdot -}(ads) \quad (2)$$

$$O_2^{\cdot -}(ads) + H^+ \rightarrow HO_2^{\cdot}(ads) \quad (3)$$

$$2HO_2^{\cdot}(ads) \rightarrow H_2O_2(ads) + O_2 \quad (4)$$

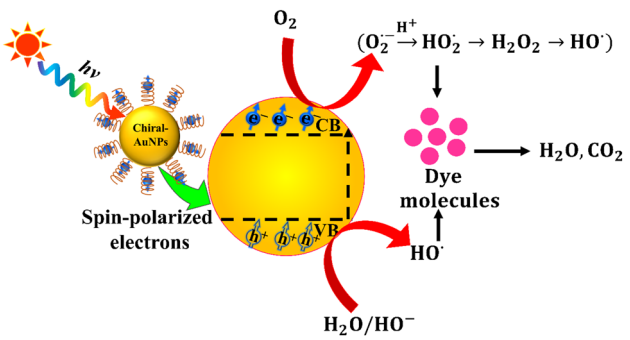

Scheme 1 A visual representation of the process of photocatalytic dye degradation.

$$H_2O_2(ads) \rightarrow 2HO^{\cdot}(ads) \quad (5)$$

$$Dye + HO^{\cdot}(ads) + HO_2^{\cdot}(ads) + O_2^{\cdot -}(ads) \rightarrow H_2O + CO_2 \text{ (dye intermediate)} \quad (6)$$

To establish our proposed mechanism that the reaction rate is enhanced due to the enhancement of the oxygen reduction reaction on the chiral catalyst surface, we have carried out the catalytic study for 4 hours in the presence of *p*-Benzoquinone as a superoxide radical ($O_2^{\cdot -}$) scavenger. The results depicted in Fig. S11 show that the degradation efficiency of photocatalytic activity is suppressed in the presence of *p*-benzoquinone in compared to the case where no scavengers are employed. These results demonstrate that the reaction passes through the reactive oxygen intermediates, which play the main role in dye degradation.

Conclusions

Hence, the experimental results manifest that chiral L- and D-Au NPs exhibit superior photocatalytic efficiency in dye degradation compared to their achiral counterparts due to the spin-polarization effect resulting from chiral-induced spin-selectivity (CISS). Furthermore, it has been observed that higher optical polarization correlates with greater spin polarization, leading to a slightly enhanced rate of dye degradation, as seen with D-Au NPs. Similar trends are observed for both cationic and anionic dyes, indicating that spin polarization plays a crucial role in the oxygen reduction process regardless of dye structure. Thus, the present study highlights a viable strategy to advance next-generation photocatalysts for sustainable environmental applications.

Author contributions

U. K. G.: investigation, methodology, formal analysis related to photocatalysis study, writing original draft. A. B.: methodology,

formal analysis related to synthesis and characterization of gold nanoparticles, writing original draft. K. B. G.: conceptualization, supervision, fund acquisition, resources, writing original draft.

Conflicts of interest

There are no conflicts to declare.

Data availability

All the data are given in the manuscript and the supporting information (SI). Raw data are available upon request from the corresponding authors. Supplementary information: synthesis methods, optical analysis, morphology study, controlled experiments, post photocatalytic study, radical trapping experiments, and error bar tables. See DOI: https://doi.org/10.1039/d6ra00665e.

Acknowledgements

U.K.G. acknowledges the FIRST Fellowship from IIT Hyderabad. A.B. acknowledges IIT Hyderabad for sponsoring the Ministry of Human Resource Development (MHRD) for the fellowship. K.B.G. acknowledges the Start-up Research Grant (SRG/2022/000737) from ANRF-India and CSIR-ASPIRE (01/WS (023)/2023-24/EMR-II/ASPIRE).

References

1 S. Dutta, B. Gupta, S. K. Srivastava and A. K. Gupta, *Mater. Adv.*, 2021, **2**, 4497–4531.
2 K. G. Pavithra, P. S. Kumar, V Jaikumar and P. S. Rajan, *J. Ind. Eng. Chem.*, 2019, **75**, 1–19.
3 M. R. Hoffmann, S. T. Martin, W. Choi and D. W. Bahnemann, *Chem. Rev.*, 1995, **95**, 69–96.
4 M. Saeed, M. Muneer, A. ul Haq and N. Akram, *Environ. Sci. Pollut. Res.*, 2022, **29**, 293–311.
5 D. Baruah, M. Goswami, R. N. S. Yadav, A. Yadav and A. M. Das, *J. Photochem. Photobiol. B Biol.*, 2018, **186**, 51–58.
6 S. Khan, T. Noor, N. Iqbal and L. Yaqoob, *ACS Omega*, 2024, **9**, 21751–21767.
7 H. Zhang, G. Chen and D. W. Bahnemann, *J. Mater. Chem.*, 2009, **19**, 5089–5121.
8 A. Ajmal, I. Majeed, R. N. Malik, H. Idriss and M. A. Nadeem, *RSC Adv.*, 2014, **4**, 37003–37026.
9 P. Song, J. Du, X. Ma, Y. Shi, X. Fang, D. Liu, S. Wei, Z. Liu, Y. Cao, B. Lin, J. Di, Y. Wang, J. Cui, T. Kong, C. Gao and Y. Xiong, *EcoEnergy*, 2023, **1**, 197–206.
10 Y. Bai, S. Li, B. Yin, J. Zhao and H. Li, *Trans. Tianjin Univ.*, 2024, **30**, 130–139.
11 Y. Sang, F. Tassinari, K. Santra, W. Zhang, C. Fontanesi, B. P. Bloom, D. H. Waldeck, J. Fransson and R. Naaman, *Proc. Natl. Acad. Sci. U. S. A.*, 2022, **119**, 1–8.
12 A. Gupta, A. Kumar, D. K. Bhowmick, C. Fontanesi, Y. Paltiel, J. Fransson and R. Naaman, *J. Phys. Chem. Lett.*, 2023, **14**, 9377–9384.
13 L. Scarpetta-Pizo, R. Venegas, P. Barrías, K. Muñoz-Becerra, N. Vilches-Labbé, F. Mura, A. M. Méndez-Torres, R. Ramírez-Tagle, A. Toro-Labbé, S. Hevia, J. H. Zagal, R. Oñate, A. Aspée and I. Ponce, *Angew. Chem., Int. Ed.*, 2024, **63**, e202315146.
14 P. Vensaus, Y. Liang, J.-P. Ansermet, G. J. A. A. Soler-Illia and M. Lingenfelder, *Nat. Commun.*, 2024, **15**, 2867.
15 J. Yan, Y. Wang, Y. Zhang, S. Xia, J. Yu and B. Ding, *Adv. Mater.*, 2021, **33**, 2007525.
16 A. Balo, U. Utkarsh, M. Yasmin, U. K. Gosh and K. B. Ghosh, *ChemCatChem*, 2025, **17**, e202401695.
17 A. Balo, M. Yasmin, U. Utkarsh, U. K. Gosh, R. Choudhury and K. Banerjee Ghosh, *ACS Appl. Energy Mater.*, 2025, **8**, 5144–5152.
18 R. Gupta, A. Balo, R. Garg, A. K. Mondal, K. B. Ghosh and P. Chandra Mondal, *Chem. Sci.*, 2024, **15**, 18751–18771.
19 R. Naaman, Y. Paltiel and D. H. Waldeck, *Nat. Rev. Chem.*, 2019, **3**, 250–260.
20 R. Naaman and D. H. Waldeck, *J. Phys. Chem. Lett.*, 2012, **3**, 2178–2187.
21 W. Mtangi, F. Tassinari, K. Vankayala, A. Vargas Jentzsch, B. Adelizzi, A. R. A. Palmans, C. Fontanesi, E. W. Meijer and R. Naaman, *J. Am. Chem. Soc.*, 2017, **139**, 2794–2798.
22 U. Utkarsh, S. R. Pramatha, A. Balo, U. K. Gosh, K. V. Rao and K. B. Ghosh, *J. Mater. Chem. A*, 2024, **12**, 20354–20363.
23 W. Zhang, K. Banerjee-Ghosh, F. Tassinari and R. Naaman, *ACS Energy Lett.*, 2018, **3**, 2308–2313.
24 U. Utkarsh, S. Sahu, A. Balo, D. Barik and K. Banerjee Ghosh, *ACS Appl. Energy Mater.*, 2025, **8**, 1722–1730.
25 D. Barik, U. Utkarsh and K. B. Ghosh, *Chem. Commun.*, 2025, **61**, 6226–6245.
26 H.-E. Lee, R. M. Kim, H.-Y. Ahn, Y. Y. Lee, G. H. Byun, S. W. Im, J. Mun, J. Rho and K. T. Nam, *Nat. Commun.*, 2020, **11**, 263.
27 R. Schillinger, Ž. Šljivančanin, B. Hammer and T. Greber, *Phys. Rev. Lett.*, 2007, **98**, 136102.
28 T. Greber, Ž. Šljivančanin, R. Schillinger, J. Wider and B. Hammer, *Phys. Rev. Lett.*, 2006, **96**, 56103.